Acta Materialia 95 (2015) 74–82

Contents lists available at ScienceDirect

Acta Materialia

journal homepage: www.elsevier.com/locate/actamat

A selective laser melting and solution heat treatment refined Al–12Si alloy with a controllable ultrafine eutectic microstructure and 25% tensile ductility

X.P. Li [a], X.J. Wang [a,b,1], M. Saunders [c], A. Suvorova [c], L.C. Zhang [d], Y.J. Liu [d], M.H. Fang [b], Z.H. Huang [b], T.B. Sercombe [a,*]

[a] The University of Western Australia, School of Mechanical and Chemical Engineering, Perth, WA 6009, Australia
[b] China University of Geosciences (Beijing), School of Materials Science and Technology, Beijing 100083, China
[c] The University of Western Australia, Centre for Microscopy, Characterisation and Analysis, Perth, WA 6009, Australia
[d] Edith Cowan University, School of Mechanical Engineering, Perth, WA 6027, Australia

ARTICLE INFO

Article history:
Received 15 January 2015
Revised 13 May 2015
Accepted 14 May 2015

Keywords:
Al–Si alloys
Selective laser melting
Solution heat treatment
Eutectic microstructure
Mechanical properties

ABSTRACT

This study shows that a eutectic Al–12Si alloy with controllable ultrafine microstructure and excellent mechanical properties can be achieved by using selective laser melting and subsequent solution heat treatment. This provides a novel and promising approach to the refinement of eutectic Al–Si alloys. Unlike Al–12Si alloys fabricated and refined by traditional methods, the as-fabricated Al–12Si in this study contains nano-sized spherical Si particles surrounding a supersaturated Al matrix. During solution heat treatment, precipitation and coalescence of the Si particles occur, which decreases the Si concentration in the matrix and sub-micron to micron-sized spherical particles embedded in an Al matrix form. The as-fabricated Al–12Si exhibits significantly better tensile properties than the traditionally produced counterparts; while the solution treated Al–12Si has an extremely high ductility of approximately 25%. Importantly, the mechanical properties of the Al–12Si can be tailored through controlling the precipitation and coalescence of the Si particles by varying the solution heat treatment time. A detailed transmission electron microscopy study was conducted to investigate this Al–12Si alloy with ultrafine eutectic microstructure. The excellent tensile properties have been attributed to the refined eutectic microstructure containing spherical Si particles. The formation of this unique microstructure is due to the super heating and an extremely high cooling rate during selective laser melting and the subsequent solution heat treatment, which enables Si to grow along its most stable plane $\{1\,1\,1\}_{Si}$.

1. Introduction

The Al–Si casting alloys are extensively used in automotive and aerospace industries due to their light weight, good mechanical properties and low recycling costs [1–3]. The mechanical properties of Al–Si alloys are largely dictated by the morphology of the eutectic silicon [4,5], with the coarse, acicular silicon acting as crack initiation sites in conventionally cast material, resulting in low ductility. As a consequence, refinement of the eutectic microstructure of Al–Si alloys, first reported in 1920 [6], has been extensively investigated [4,7–13] since and is a critical step in improving their mechanical properties (specifically strength and ductility) to meet the ever-growing application demands in automotive and aerospace industries. This is becoming more imperative as the worldwide energy and environment problems worsen.

The refinement of the Si phase can be achieved by controlling the nucleation and growth of the eutectic grains. Usually, two different methods of refinement are used: elemental additions [14–17] and rapid solidification [18–21]. Although the use of chemical elements can result in reduced fluidity and higher cost, its major disadvantage is the rapid loss of the refining elements from evaporation or oxidation [22]. In addition, the selection of appropriate elements depends on many factors, such as the composition of the alloy, type and quantity of the modifying elements and interactions between the modifying elements. Thus, this modification approach is complex and sometimes hard to control. For example, it has been reported that the combined addition of Sr and Na does not further enhance the modification effect on the eutectic microstructure of a hypoeutectic Al–Si alloy due to the loss of

* Corresponding author.
E-mail address: tim.sercombe@uwa.edu.au (T.B. Sercombe).
[1] Shandong Academy of Sciences, Jinan, Shandong Province, China.

http://dx.doi.org/10.1016/j.actamat.2015.05.017
1359-6454/

modifying elements as a result of vaporisation or oxidation promoted by Na [22]. In contrast, a combined addition of Sr and B into near-eutectic Al–Si alloys can significantly decrease the size of the eutectic grains at a cooling rate of 10 K/s [12]. The addition of B varies the nucleation mechanism of the eutectic, while Sr increases the undercooling of the melt. However, the addition of modifying elements can be detrimental to the density of the alloys by inducing a higher porosity. This has been attributed to the changes in hydrogen content, oxide permeability and surface tension [9].

An alternate approach to refine the microstructure is to increase the cooling rate [23,24]. Rapid solidification can significantly improve the mechanical properties of cast Al–Si components [25]. However, microstructural uniformity is only possible if the entire casting solidifies at a high cooling rate. For the vast majority of castings, this is not possible and therefore this method of Si refinement is limited to small, thin parts, such as ribbons, filaments and flakes [19–21]. For example, melting spinning has been successfully used to modify the eutectic microstructure of some Al–Si alloys [26,27]. Although submicron or nano-sized Si particles (50–200 nm) formed, the size and geometry of samples are severely constrained, with only ribbons (thickness $\leqslant$ 200 μm) or small rods able to be produced. This greatly limits the possible applications of melt spinning. To circumvent the abovementioned drawbacks and realise the thermal modification of eutectic microstructure in a large scale part, selective laser melting (SLM), an emerging additive manufacturing technique, is adopted. SLM fabricates components layer by layer, which enables the fabrication of complex-geometry components [28]. Due to the laser heating only a very small volume of material and the short laser interaction time, the process has very high heating and cooling rates (10^3–10^8 K/s) [29] which has been shown to result in the formation of metastable phases [30,31]. Following this, the high heating and cooling rate would induce large super heating and undercooling and this will tend to enhance the nucleation rate and suppress the grain growth in the Al–Si alloy. This unique characteristic makes SLM a promising candidate for producing a refined microstructure and therefore enhanced properties. In recent work [32], the annealing of Al–12Si samples produced by SLM was performed at temperatures $\leqslant$450 °C for 6 h. This work concluded that the microstructure becomes coarser with increasing annealing temperature, which led to an increase in ductility (elongation ~15%) and decrease in strength (~95 MPa). Rietveld analysis was performed on X-ray diffraction (XRD) data, which showed that the as-processed Al matrix was supersaturated in Si, which was rejected during heat treatment.

In this study, we perform a systematic investigation into the influence of selective laser melting and subsequent conventional solution heat treatment on the eutectic microstructure and on the resultant mechanical properties of Al–12Si alloy. A detailed transmission electron microscopy (TEM) investigation of the eutectic microstructure of the Al–12Si alloy which exhibits excellent mechanical properties (elongation ~25% with a tensile strength ~190 MPa) after solution heat treatment has also been conducted. The relationship between the SLM processing, eutectic microstructure and mechanical properties is discussed. A possible underlying mechanism for the formation of this novel eutectic microstructure is also proposed. This study provides new insights into the modification of Al–Si alloys through SLM and solution heat treatment to achieve the desired mechanical properties without the need for the addition of other elements.

2. Experimental procedures

2.1. Fabrication and solution treatment of Al–12Si specimens

Al–12Si specimens ($4 \times 4 \times 4$ mm^3) and tensile bars (shown in Fig. 1) were produced on a ReaLizer SLM-100 machine (ReaLizer GmbH, Germany) which is equipped with a fibre laser, which has a laser wavelength of 1.06 μm and maximum power of 200 W at the part bed. Al–12Si (in wt.%) powder ($d_{50} \sim 38$ μm, TLS Technik, Germany) was used. An inert, high purity argon gas atmosphere was used during processing to minimise oxidation. The laser scan speed and laser power were 500 mm/s and 200 W, respectively, which has been shown to produce the best properties [33]. The powder layer thickness was fixed at 50 μm and the scan spacing at 150 μm, while the substrate was heated to 200 °C. Solution heat treatment of specimens was performed in air at 500 °C for up to 4 h, followed by water quenching.

2.2. Microstructure and mechanical properties characterisation

The eutectic microstructure of the Al–12Si specimens after both fabrication and solution heat treatment was characterised using a FEI Verios 460 scanning electron microscope (SEM, acceleration voltage 5 kV, working distance 6 mm). The size and morphology of the Si particles were investigated by imaging analysis software Image Pro Plus. At least ten different regions on each sample were taken for image analysis.

The growth of Si particles, orientation relationship (OR) between Si and Al and the chemical analyses of the Al–12Si specimens were investigated using either a JEOL 2100 transmission electron microscope (TEM) or FEI Titan G2 80–200 TEM with ChemiSTEM technology at 200 kV. TEM samples were mechanically polished and finally thinned by a Precision Ion Polishing System (Gatan PIPS™) where low-angle and low-current polishing conditions were used in conjunction with a liquid nitrogen cold stage.

The residual stresses within the Al–12Si alloy before and after the solution heat treatment were characterised by the Raman peak shift of the Si [34]. Raman spectra were acquired at room temperature with a confocal Raman backscattering technique (WITec alpha 300RA+) using a 532 nm excitation wavelength. The laser light was coupled into the microscope using a single-mode fibre and brought on to the sample using a dichroic mirror and a 100× microscope objective (NA 0.9). The spatial resolution is about 100 nm with a spectral resolution of 0.02 cm^{-1}.

Tensile tests were carried out on machined specimens (gauge length ~$4 \times 6 \times 15$ mm^3), using an Instron 5982 machine at a constant strain rate of 1 mm/min. Strain was measured with a 10 mm gauge length extensometer. Samples were aligned perpendicular to the build direction as shown in Fig. 1.

2.3. Estimation of temperature distribution during SLM

Since the laser–material interaction time is usually on the order of 100 μs and the interaction volume is less than 50 μm, it is not practical to measure the temperature distribution within the Al–12Si melt pool during SLM. Therefore, a finite element modelling

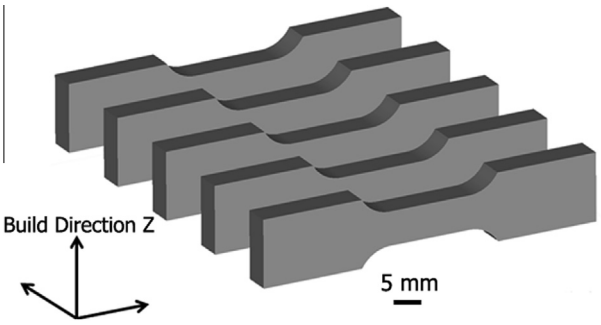

Fig. 1. A schematic illustration showing the orientation of the tensile bars and the axis system used.

(FEM) method using a multi-physics-based computational model based on the heat transfer theory in the heat transient mode of COMSOL™ was used to estimate the temperature distribution. For Al–12Si alloys, the laser absorption is very low ~5% at the 1.06 μm wavelength used [35]. However, many factors such as the size and morphology of the powder particles, the surface and roughness of the samples will influence the actual absorption co-efficient of a material. In general, the laser absorption for a powder sample is 3–5 times higher than a thin film sample with the same composition [36,37]. Therefore, in this work, the absorption co-efficient was set to 20%. For simplification, the simulation was carried out on an Al-based thin film with the same composition as the powder and there was no gap between the last and current layer. The thickness of this thin film was set to 100 μm. The laser power and scan speed were set to be 200 W and 500 mm/s in the simulation, respectively, the same value as we used for the SLM processing.

3. Results and discussion

3.1. Eutectic microstructure after SLM and upon solution heat treatment

The microstructure of the Al–12Si alloy in the as-processed condition and after different solution heat treatment times is shown in Fig. 2. Unlike the eutectic microstructure of cast Al–12Si alloys where large rod- or needle-like Si particles form in the Al matrix, a novel eutectic microstructure with very fine spherical Si particles has formed, as shown in Fig. 2a. Two distinct regions can be observed: one significantly coarser than the other. This indicates that these two regions have different thermal histories. It has been reported [38] that the microstructure of Selective Laser Melted aluminium is affected by the heat generated by both the overlapping scan lines and creation of subsequent layers. Both these processes cause localised partial heat treatment and coarsening of the microstructure, as shown in Fig. 2a. Upon solution heat treatment, it can be seen (Fig. 2b–e) that the eutectic Si particles have grown and are up to ~2 μm in diameter. After solution heat treatment the abovementioned differences in the scale of the microstructure appear much less distinct; both larger and smaller Si particles distribute relatively homogeneously in the Al matrix.

To investigate the changes in size and morphology of the eutectic Si particles upon solution heat treatment, detailed image analysis was conducted on SEM images obtained after different solution treated times. Results are shown in Fig. 3 and Table 1. It can be seen from Fig. 3 and Table 1 that when the Al–12Si was solution treated less than 30 min most of the Si particles are less than 1 μm and particles below 0.16 μm account for 50% of the total Si particles. After longer solution heat treatment times (from 30 min up to 2 h), some of the Si particles have coarsened to a diameter of ~2 μm, increasing the d_{90} in Table 1. However, it appears that times longer than 2 h have no significant effect on the size of the Si particles. Although there are larger Si particles that form after 2 h solution heat treatment, Si particles less than 0.2 μm can still be observed in the Al matrix and account for 50% of the total Si particles observed. Hence it appears that some of the smaller Si particles that have formed in the microstructure remain almost unchanged through subsequent solution treatment, while others coarsen as would be expected. This leads us to presume that the growth of the eutectic Si particles, apart from the impact of different thermal histories during SLM, may also be influenced by the chemical inhomogeneity within the as-processed alloy. This is detailed further is Section 3.2 below.

During the early stages of solution treatment, the number of Si particles decreases while the total area of Si increases as shown in Fig. 3. The decrease in the number of particles is likely a result of both particle coalescence as well as Ostwald ripening, where the large particles grow at the expense of the small ones. An increase in the area fraction of Si particles indicates that in the as-processed condition, the Al matrix is supersaturated and during heat treatment the excess Si precipitates out. It is apparent that most of the Si particles after solution treatment remain spherical, with only a small fraction becoming elongated particles.

3.2. Si content in the Al matrix

It is well known that rapidly cooling an alloy can result in significant extended (non-equilibrium) solid solubility. The eutectic structure as shown in Fig. 2 consists of cellular Al grains which are surrounded by Si particles with a spherical morphology and less than 100 nm in diameter. This structure is similar to those reported in Al–Si alloy specimens fabricated by melt spinning [26,27], where the reported Si content in the Al matrix reaches about 6% after the rapid solidification. The content of Si in the Al matrix before and after solution heat treatment was measured using TEM energy-dispersive X-ray spectroscopy (EDX) mapping. Fig. 4 shows the mapping results in scanning transmission electron microscopy (STEM) mode of the distribution of Al and Si in the as-fabricated and solution treated Al–12Si alloys. A quantitative analysis of the results shows that in the as-fabricated condition, the Si content was ~7 wt.% in the Al, which far exceeds the maximum solubility of 1.6 wt.% and is even slightly greater than what has been reported in melt spinning [26,27]. However, upon solution treatment the Si content in the Al drops rapidly to ~2 wt.% after just 15 min and then to the equilibrium concentration of 1.6 wt.% after 30 min, as shown in Fig. 4f. Longer solution treatment times have no influence on the Si content in Al, which remains ~1.6 wt.%. Hence it appears that after very short solution treatment times (⩽15 min), the supersaturated Si precipitates from the Al to form tiny eutectic Si particles, as can be seen from Figs. 2b and 4b. Upon further solution heat treatment, the Si content in the Al matrix drops to the equilibrium concentration and therefore no more precipitation of Si occurs and the area fraction of Si remains constant (Fig. 3). However, continued growth of the Si particles occurs at longer times most likely through a combination of Ostwald ripening and coalescence of adjacent small Si particles, which can be seen from the initial joining neck between two neighbouring Si particles in Fig. 4c and the elongated shape of the large Si particles in Fig. 4d and e.

3.3. Mechanisms for the formation and growth of eutectic Si particles

It is known that the solidification microstructure of Al–Si alloys can be influenced by super heating with a finer and/or more uniform microstructure along with increased strength and ductility in samples that have undergone significant superheat prior to solidification [39–43]. The underlying reason has been attributed to the existence of two characteristic temperatures, the dissolution temperature T_d and the branching temperature T_b. Below T_d, the liquid contains aluminium and silicon-rich particles which have been inherited from the solid material. Once the T_d has been exceeded, these particles begin to melt and above the branching temperature, T_b, molten alloy can be considered homogenous. Between T_d and T_b, Al-rich and Si-rich regions 10–200 nm in size co-exist within the molten pool [39]. This inhomogeneous microstructure will remain in the solidified alloys if the cooling rate is high enough ($\geqslant 10^3$ K/s). According to previous studies, T_d and T_b of Al–12Si alloys should be around 1080 ± 30 and 1290 ± 30°C, respectively [39,44]. This temperature is much higher than the liquidus temperature of Al–12Si alloys (577 °C). Given that measuring the temperature in the melt pool in such a short

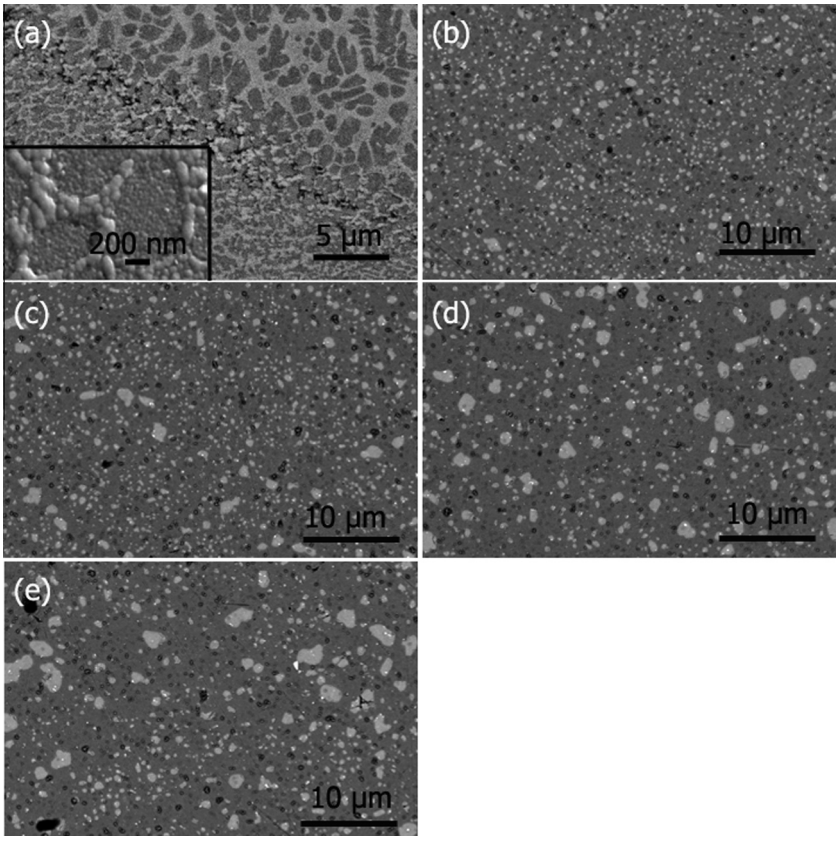

Fig. 2. Back-scattered SEM images of the eutectic microstructure of the Al–12Si alloy in the (a) as-fabricated condition in which the two distinct regions in the as-fabricated Al–12Si alloy: coarse Si and fine Si regions can be observed and after solution treatment at 500 °C for (b) 15 min; (c) 30 min; (d) 2 h; and (e) 4 h. The light grey areas are Si particles. The inset in (a) is high resolution secondary electron image showing that the Si forms small ~50 nm particles. Note the scale bar in (a) is different from the scale bars in (b) to (e).

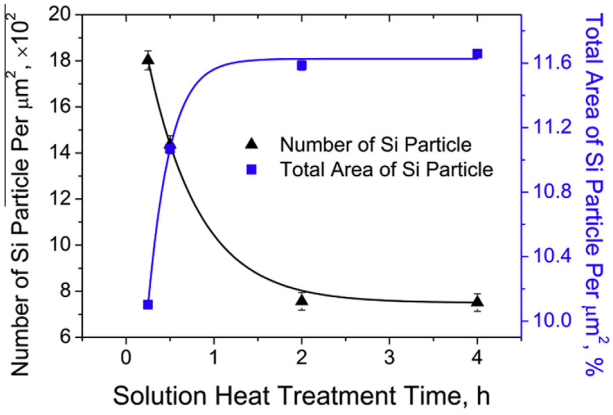

Fig. 3. The Si particle number and total Si particle area as a function of solution treatment time based on the SEM images shown in Fig. 2.

Table 1
Summary of the eutectic Si particle size (μm) in the Al–12Si alloy with different solution heat treatment times. d_x (x = 10, 50 or 90) means x% of the Si particles has a diameter less than d_x. $\overline{d}$ means the average diameter.

Solution heat treatment time	d_{10} (μm)	d_{50} (μm)	d_{90} (μm)	$\overline{d}$ (μm)
15 min	0.11	0.16	0.47	0.23
30 min	0.11	0.17	0.68	0.27
2 h	0.11	0.20	0.77	0.36
4 h	0.11	0.20	0.78	0.36

time is currently not possible, the temperature distribution upon heating within the melt pool in this study was estimated based on the transient heat transfer model using COMSOL™ [45] (the details of the approach have been given previously [46]) and the results are shown in Fig. 5. The maximum temperature is at the centre of the molten pool and reaches about 1439 °C, which lies above T_b of Al–12Si alloy. However, it can be seen that the temperature of a large portion of the melt pool lies in between T_d and T_b of Al–12Si alloy (see the shaded area in Fig. 5a). Hence, a large portion of the Al–12Si alloy melt pool probably undergoes a super heating in the temperature range between T_b and T_d. This will lead to an inhomogeneous microstructure of the molten pool of Al–12Si. In addition, the short interaction time between laser and material and the formation of liquid oscillations or capillary waves will also tend to make the microstructure within the molten pool inhomogeneous [47]. Hence, an inhomogeneous microstructure consisting of nano-sized Al-rich and Si-rich regions is expected, benefiting the heterogeneous nucleation and enhancement of the nucleation rate. The cooling rate is also estimated (based on the simulation) to be above 10^3 K/s for most parts of the melt pool, as shown in Fig. 5b. This super-high cooling rate will help retain the abovementioned inhomogeneous microstructure. Therefore, Si particles around 10–100 nm in size and a supersaturated Al matrix are expected to form in the as-fabricated Al–12Si alloy, and has been observed as shown in Fig. 4a. The growth of these nano-sized Si particles within the microstructure of the as-fabricated Al–12Si alloy upon heat treatment is further discussed below.

Fig. 6a shows energy filtered TEM (EFTEM) images of the eutectic Si particles embedded in the Al matrix after heat treatment for 15 min at 500 °C. The spherical Si particles have a diameter of less

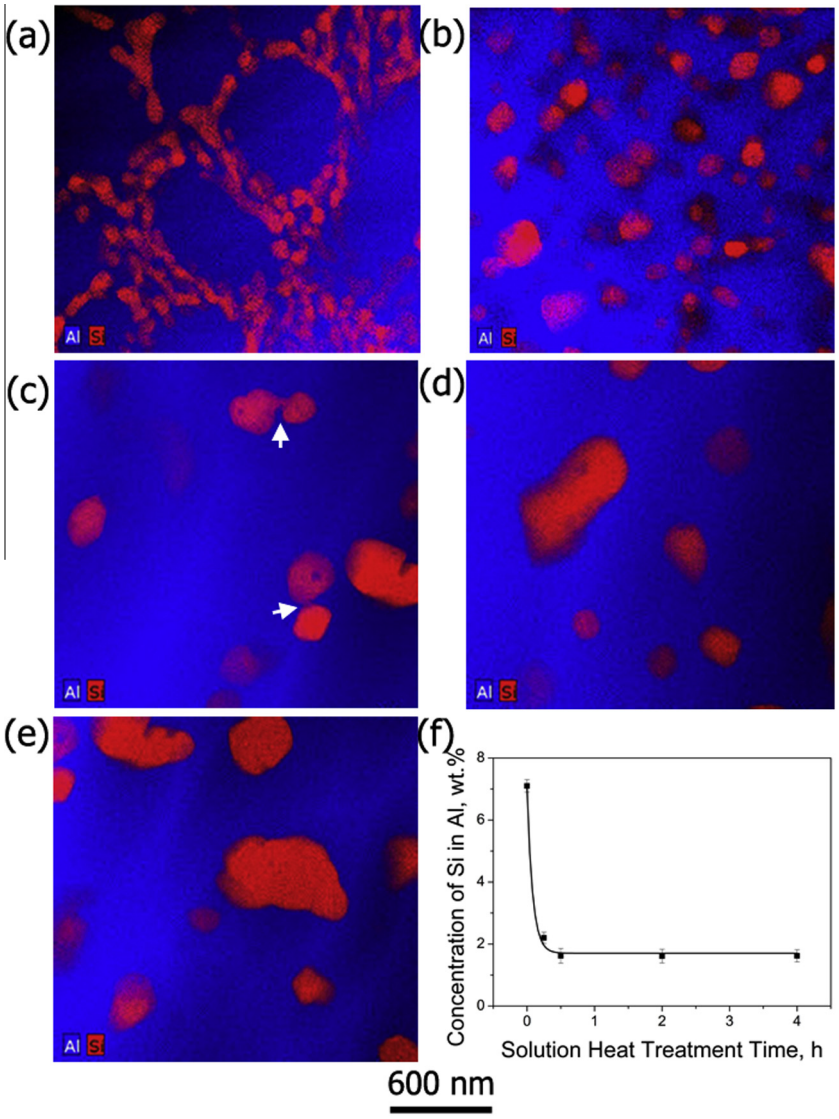

Fig. 4. STEM-EDX maps of the Al and Si distribution in the Al–12Si alloy in the (a) as-fabricated condition and after solution treatment at 500 °C for (b) 15 min; (c) 30 min; (d) 2 h; and (e) 4 h; (f) Concentration of Si in Al at different solution heat treatment times. White arrows in (c) shows the position of the joining neck between adjacent Si particles.

than 100 nm and are located at the Al grain boundaries. The electron energy loss spectroscopy (EELS) spectra of the Al grain and Si particle are shown in Fig. 6b, where the onset and shape of the ionisation edges for the Al grain and Si particles illustrates the valence and bonding state for Al atoms and Si atoms in these two regions. No Si particles are observed inside the Al grains, which indicates that during solution heat treatment, precipitation of the excess Si in the Al matrix occurs at the Al grain boundaries. This is consistent with the results shown in Fig. 4b and further implies that the growth or coalescence of the Si particles also occurs along the Al grain boundaries.

The morphology of the eutectic Si phase, which is directly related to its nucleation and growth processes, is critical in modifying the mechanical properties of Al–12Si alloy. Apart from the interfacial energy $\gamma^{Al/Si}$ between Al and Si phases, other kinetics or thermodynamic factors such as the wettability (normally expressed by the contact angle θ_c) and the local concentration of Al and Si atoms also play a key role in determining the eutectic microstructure upon solidification [9,48,49]. During conventional casting or for a cooling rate below 10 K/s, the growth direction of eutectic Si is usually $\langle 110 \rangle$ or $\langle 100 \rangle$ [50] and forms a rod- or needle-like coarse microstructure (usually tens to hundreds of microns in size). This rod-like and needle-like morphology with its coarse microstructure is well known to severely reduce the ductility of Al–12Si alloys. In contrast, the spherical, nano-sized eutectic Si in our materials results in enhanced mechanical properties, especially ductility [9]. To investigate the underlying mechanism for the formation of the rounded eutectic Si, the orientation relationship (OR) between Al grains and Si phases has been determined. The interface between the Al and Si particle is shown in the bright field (BF) TEM image in Fig. 7a. The interface was tilted to edge-on position and overlapped diffraction patterns were taken at the boundaries of Al and Si, as shown Fig. 7b. Both Al and Si have a cubic structure and the OR determined from Fig. 7b can be expressed as $(111)_{Si}||(200)_{Al}$. A high resolution TEM (HRTEM) image is taken along the same zone axis, shown in Fig. 7c, where the parallel lattice fringes of the $(111)_{Si}$ and $(200)_{Al}$ planes can be clearly seen at the interface between Al and Si phases. It shows that an epitaxial relationship exists between the eutectic Si and Al. This is different from previously reported observations at low

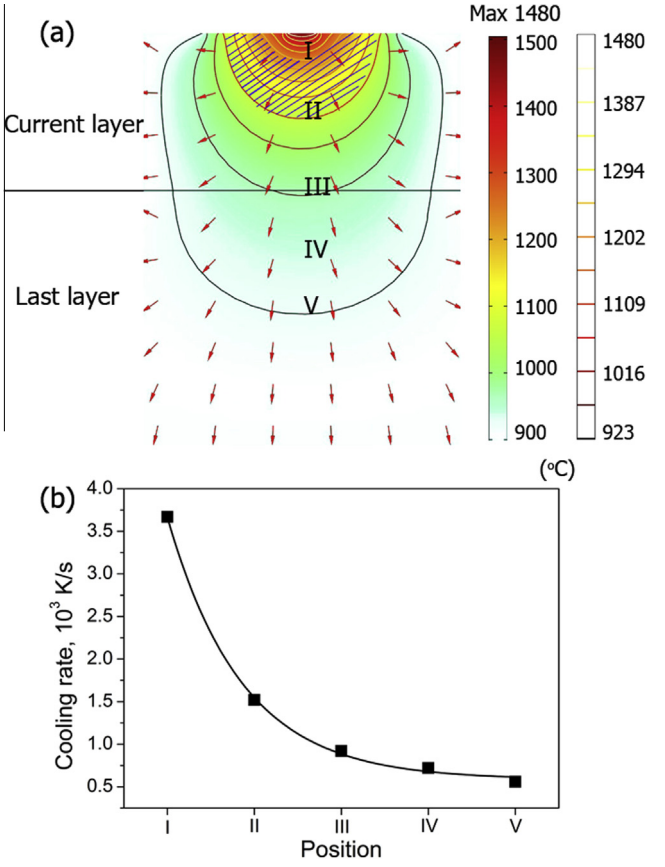

Fig. 5. (a) Temperature distribution of the Al–12Si molten pool upon heating during SLM based on COMSOL™ modelling. (b) Estimated cooling rates at the positions marked *I*–*V* in (a). Red arrows schematically show the direction of heat transfer. Shaded area shows the region of the melt pool undergoing a temperature between T_b and T_d. (For interpretation of the references to colour in this figure legend, the reader is referred to the web version of this article.)

temperature or at low cooling rate, where the Si particle grows within the dendrite microstructure of Al grains, especially at the arms and tips of the dendrite [9].

In this study, the Si and Al form Si-rich and Al-rich regions in the melt with a size below 100 nm. Upon rapid cooling, these regions are mostly retained and the growth during cooling is greatly restrained. When heat treated at a high temperature, the Si phase undergoes a thermally activated growth process. This enables the Si phase to grow along the most stable plane with the lowest free energy: the most dense-packed plane $\{1\,1\,1\}_{Si}$. This is why the Si phase grows into a spherical morphology.

3.4. Residual stress

The high heating and cooling rate experienced during SLM causes high temperature gradients and thermal fluctuations to occur [51]. This results in severe thermal and residual stresses to form within the fabricated components [51], which has been characterised by the Raman peak shift of Si within the Al–12Si alloy [34]. Fig. 8 shows the position of the Raman peak of Si in the as-processed Al–12Si alloy and solution treated Al–12Si with different times. The corresponding Raman intensity mapping results are also shown as inset in Fig. 8. The lower wave number of the Si line (~517.6 cm^{-1} compared with 520.7 cm^{-1} stress-free Si [52]) in the as-fabricated Al–12Si alloy indicates that the Si in the as-fabricated Al–12Si alloy contains significant residual tensile stresses. The Raman shift becomes smaller upon solution treatment, implying that the stress is relaxed through solution treatment. These residual stresses together with the nano-sized Si particles and ultrafine Al matrix in the as-fabricated Al–12Si alloy would introduce a large number of dislocations and boundaries into the components. These dislocations and boundaries could act as paths for fast diffusion which is critical to precipitation and growth of the Si particles. Compared to conventionally fabricated Al–Si alloys, this substantial diffusivity can lead to enhanced recovery which also benefits the tensile ductility or stable plasticity.

3.5. Mechanical properties

The variation of the mechanical properties of the fabricated Al–12Si alloy after different solution heat treatment times is shown in Fig. 9. It has been previously reported that the as-fabricated properties exceed that of castings [33]. After solution heat treatment of

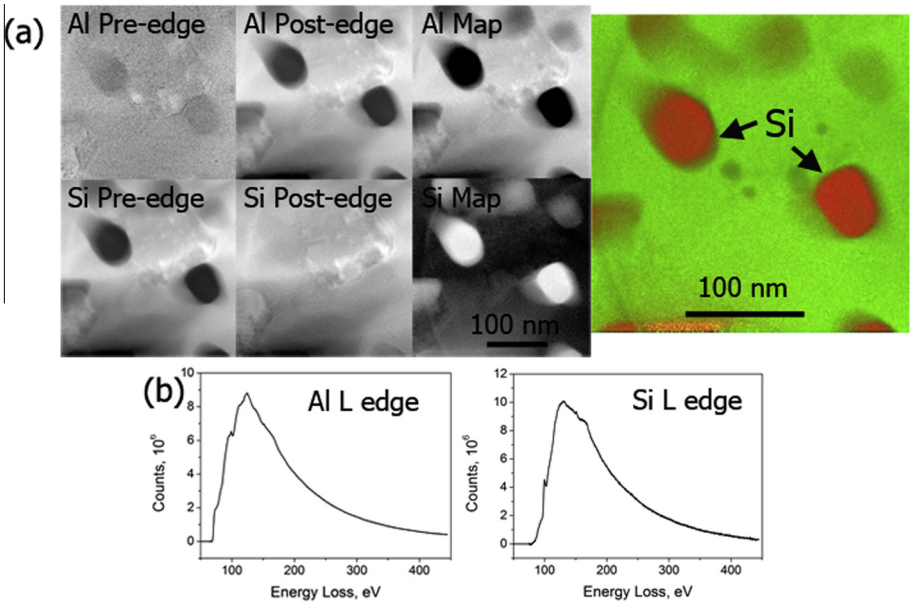

Fig. 6. (a) EFTEM images of the eutectic Si particles embedded in the Al matrix after solution heat treatment for 1 h at 500 °C. (b) EELS spectra of the Al grain and Si particle.

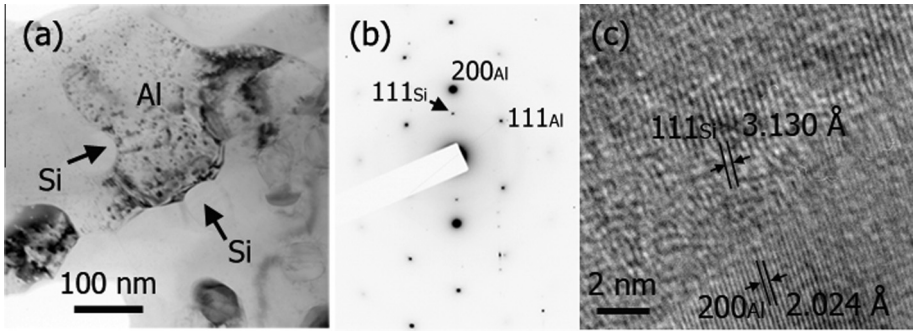

Fig. 7. (a) A bright field TEM image showing the interface between Al grain and Si particles. (b) A selected area diffraction pattern taken at the interface when tilted to edge-on position. (c) A HRTEM image showing the epitaxial relationship of Si.

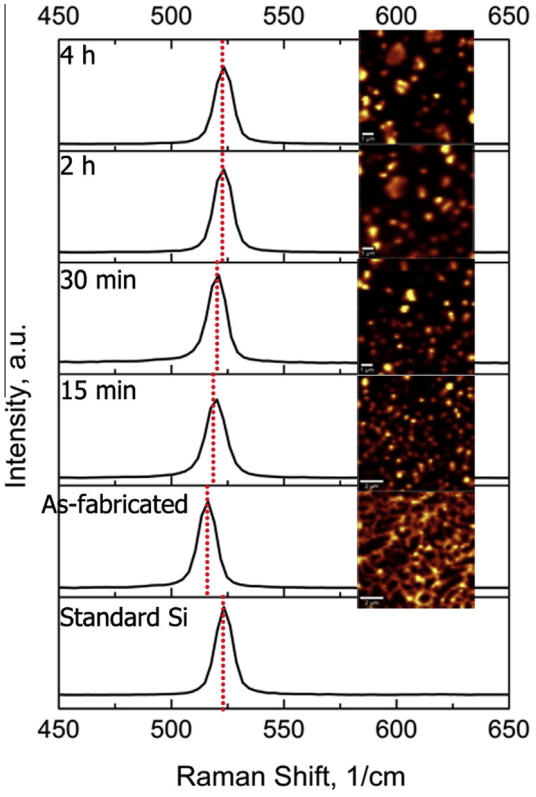

Fig. 8. Raman spectra from the Si particles in the Al–12Si alloys solution treated with different times. Inset shows the Raman intensity mapping of the corresponding Al–12Si alloys measure in the region of 500–550 cm^{-1}. The Raman spectrum for a standard Si is also shown. There is a gradual increase in the Raman shift during heat treatment.

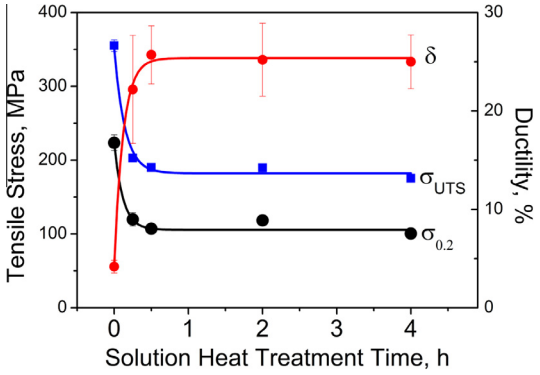

Fig. 9. The variation of mechanical properties of the Al–12Si alloy upon solution heat treatment at different times. δ, $\sigma_{0.2}$ and σ_{UTS} represent the ductility, yield strength and ultimate tensile strength, respectively.

just 15 min, a large increase in ductility and decrease in strength can be observed. When further increasing the solution treatment time to 30 min, the elongation increases to about 25% and the yield and tensile strength decreases to approximately 110 and 190 MPa, respectively. However, no further change in the mechanical properties occurs after longer times. It seems that the mechanical properties of the Al–12Si reach a plateau after 30 min solution heat treatment.

Fig. 10 shows the fracture surface of the Al–12Si alloys before and after solution heat treatment. A typical brittle failure with regular cleavage planes can be seen in the as-fabricated Al–12Si alloy, which is consistent with the low ductility shown in Fig. 9. When the material has been heat treated for just 15 min, equiaxed dimples with an average size around 2 μm were observed across the whole fracture surface, as shown in Fig. 10b, which is indicative of a highly ductile fracture. As the solution treatment time is increased further, the size of the equiaxed dimples increases (Fig. 10c–e) and are approximately 5 μm after 4 h. A careful observation shows that the edges of the dimples pass through both Al grains and eutectic Si particles, signifying that the eutectic Si particles no longer act as the main sites triggering fracture.

It is well recognised that the size and morphology of the eutectic Si particles have an important impact on the mechanical properties of the Al–Si alloys [9]. In the conventional casting of Al–Si alloys, due to the faster growth rate of the Si phase compared to the Al phase during solidification, plate-like, rod-like and needle-like eutectic Si phases tend to form in the Al matrix [4,9]. In tensile loading, this kind of morphology of Si phases causes localised shearing to occur at a very early stage of the plastic deformation. This localised shearing can easily initiate cracks and promote crack propagation, triggering a fast fracture with a nominal plastic strain of only a few per cent. In the present study the nano-sized spherical Si particles that form in the as-fabricated Al–12Si alloy can ease the localised shearing and hence suppress the crack initiation and propagation. Therefore, there is enhanced tensile ductility in the as-fabricated Al–12Si components compared with cast material. The high strength of the as-processed material is likely a result of the non-equilibrium solubility of Si in the Al matrix as well as the refinement of the eutectic Si particles and ultrafine Al matrix. However, the relative contribution of these three factors to the enhancement of tensile strength is still unknown.

The influence of solution heat treatment on the strength and ductility of Al–Si alloys is dictated by many factors such as number, morphology and size of the Si phases, initial hardening rate and

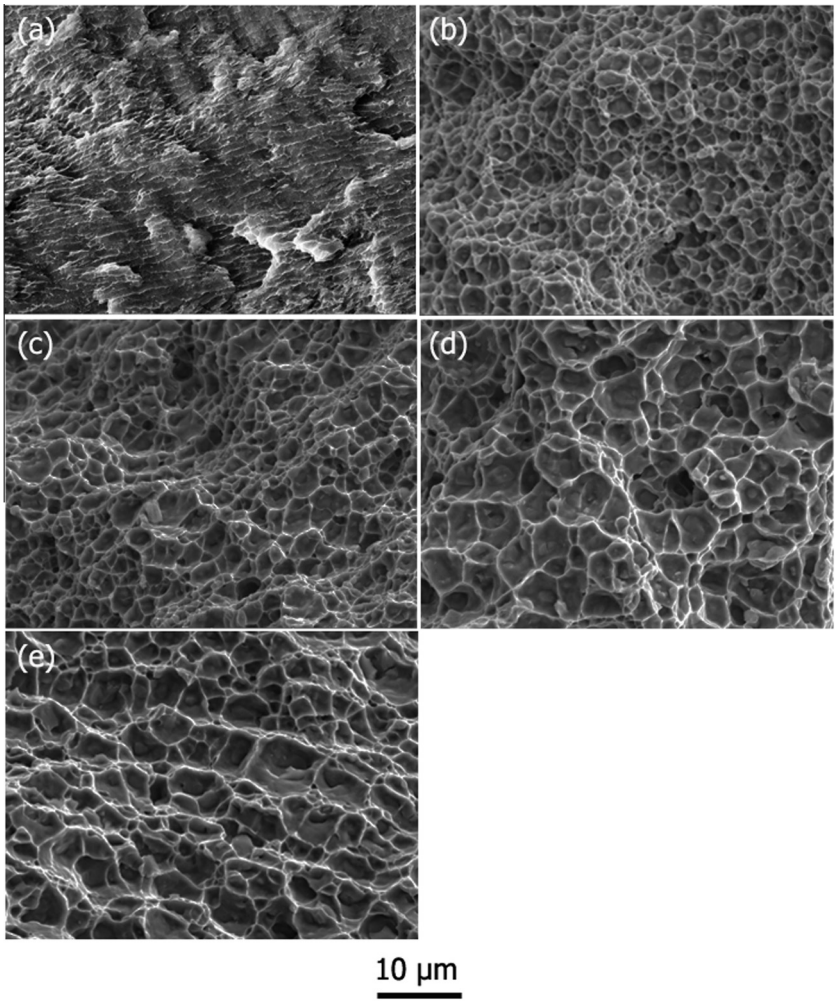

Fig. 10. SEM images (secondary electron images) of the fracture surface of the Al–12Si alloys with different solution heat treatment times (a) as-fabricated; (b) 15 min; (c) 30 min; (d) 2 h; and (e) 4 h, respectively.

recovery rate [53]. The last two factors are closely related to the solute content in the solid solution, which in this study is the Si content in the Al matrix. Upon solution treatment, the Si trapped in the Al matrix rapidly precipitates out onto the existing Si particles which sit at the Al grain boundaries, as shown in Fig. 7, thus reducing the solid solution strengthening. This also results in an increase in the volume fraction of Si (Fig. 3). The Si particles also coarsen during the early phases of the heat treatment through both coalescence of small Si particles as well as Ostwald ripening, which result in both an increase in size (Table 1) and decrease in the number of particles (Fig. 3). However, these processes appear to stop after ~2 h and the system reaches equilibrium. All of these together act to reduce tensile strength of the Al–12Si components. The Si content (and hence solid solution strengthening it creates) in the Al matrix drops rapidly during solution heat treatment and remains constant for times longer than 30 min. Hence, the strength of the Al–12Si also drops abruptly and is constant for times greater than 30 min. As to the tensile ductility of the solution treated Al–12Si alloys in this study, two aspects need to be considered. Firstly, the decrease in the number of Si particles and increase in size favour the reduction of localised stress or strain. Secondly, solution treatment reduces the residual stresses which have built up during the SLM process (Fig. 8). These two aspects benefit the enhancement of the tensile ductility of the solution treated Al–12Si components [1].

4. Conclusion

In this work, we have shown that, similar to melting spinning, selective laser melting (SLM) features rapid cooling rates during processing. This enables the formation of an ultrafine eutectic microstructure in an Al–12Si alloy. Unlike the eutectic microstructure observed in Al–12Si alloys fabricated by conventional methods or refined by addition of minor elements, the eutectic microstructure is characterised by spherical nano-sized Si particles embedded in the Al matrix. This ultrafine eutectic microstructure gives rise to significantly better tensile properties compared to traditionally fabricated Al–12Si parts.

Upon solution treatment, the size of the eutectic Si particles, which are critical to the mechanical properties of Al–12Si parts increases with increasing the solution treatment time. The bimodal distribution of the Si particle size is retained. However, the coarse and fine Si particles distribute homogenously in the Al matrix. Based on the detailed TEM study, it was found that spherical Si particles with a diameter below 100 nm formed at the Al grain boundaries as a result of the extremely high cooling rate during SLM. Together with the inhomogeneous chemical distribution, this enables the Si to grow along its most stable plane $\{1\,1\,1\}_{Si}$ during solution treatment. This micro-sized eutectic microstructure was believed to be the underlying reason for the very high tensile ductility ~25% of the Al–12Si alloy.

This study shows that Al–12Si alloy with exceptional tensile properties and ultrafine eutectic microstructure can be obtained by selective laser melting and subsequent solution treatment. The eutectic microstructure of Al–12Si alloys, especially the size of the Si particles, can be tailored effectively by varying the solution treatment time. This provides important insights into refinement of Al–Si alloys without the addition of other elements.

Acknowledgements

This work was supported by the Australian Research Council (ARC) Discovery Project DP130103592 and ECM Research Development Grant, The University of Western Australia (UWA). The authors also acknowledge the facilities, and the scientific and technical assistance of the Australian Microscopy & Microanalysis Research Facility at the Centre for Microscopy, Characterisation & Analysis, The University of Western Australia, a facility funded by the University, State and Commonwealth Governments.

References

[1] I. Gutierrez-Urrutia, M.A. Munoz-Morris, D.G. Morris, Acta Mater. 55 (2007) 1319–1330.
[2] M.A. Moustafa, F.H. Samuel, H.W. Doty, J. Mater. Sci. 38 (2003) 4523–4534.
[3] B. Li, H. Wang, J. Jie, Z. Wei, Mater. Des. 32 (2011) 1617–1622.
[4] S.D. McDonald, K. Nogita, A.K. Dahle, Acta Mater. 52 (2004) 4273–4280.
[5] Y.-C. Tsai, C.-Y. Chou, S.-L. Lee, C.-K. Lin, J.-C. Lin, S.W. Lim, J. Alloys Compd. 487 (2009) 157–162.
[6] Pacz A. Alloy. US Patent 1387900. 1921.
[7] P. Mohanty, J.E. Gruzleski, Acta Mater. 44 (1996) 3749–3760.
[8] D. Qiu, J.A. Taylor, M.X. Zhang, P.M. Kelly, Acta Mater. 55 (2007) 1447–1456.
[9] S. Hegde, K.N. Prabhu, J. Mater. Sci. 43 (2008) 3009–3027.
[10] J. Asensio-Lozano, B. Suarez-Pena, Scripta Mater. 54 (2006) 943–947.
[11] X. Jian, T.T. Meek, Q. Han, Scripta Mater. 54 (2006) 893–896.
[12] H. Liao, M. Zhang, Q. Wu, H. Wang, G. Sun, Scripta Mater. 57 (2007) 1121–1124.
[13] B. Suarez-Pena, J. Asensio-Lozano, Scripta Mater. 54 (2006) 1543–1548.
[14] H.Y. Geng, Y.X. Li, C. Xiang, W. Xue, Scripta Mater. 53 (2005) 69–73.
[15] S. Farahany, A. Ourdjini, T.A. Abu Bakar, M.H. Idris, Metall. Mater. Trans. A 45 (2014) 1085–1088.
[16] F. Wang, Z. Liu, D. Qiu, J.A. Taylor, M.A. Easton, M.-X. Zhang, Acta Mater. 61 (2013) 360–370.
[17] K. Narayan Prabhu, B.N. Ravishankar, Mater. Sci. Eng., A 360 (2003) 293–298.
[18] L. Pedersen, L. Arnberg, Metall. Mater. Trans. A 32 (2001) 525–532.
[19] Y. Birol, J. Alloys Compd. 439 (2007) 81–86.
[20] A.M. Bastawros, M.Z. Said, J. Mater. Sci. 28 (1993) 1143–1146.
[21] Y. Birol, J. Mater. Sci. 31 (1996) 2139–2143.
[22] L. Lu, K. Nogita, A.K. Dahle, Mater. Sci. Eng., A 399 (2005) 244–253.
[23] R. Trivedi, F. Jin, I.E. Anderson, Acta Mater. 51 (2003) 289–300.
[24] M. Gremaud, D.R. Allen, M. Rappaz, J.H. Perepezko, Acta Mater. 44 (1996) 2669–2681.
[25] E. Karakoese, M. Keskin, J. Alloys Compd. 479 (2009) 230–236.
[26] Z. Chen, Y. Lei, H. Zhang, J. Alloys Compd. 509 (2011) 7473–7477.
[27] J.H. Li, M.Z. Zarif, G. Dehm, P. Schumacher, Philos. Mag. 92 (2012) 3789–3805.
[28] D.D. Gu, W. Meiners, K. Wissenbach, R. Poprawe, Int. Mater. Rev. 57 (2012) 133–164.
[29] T. Vilaro, V. Kottman-Rexerodt, M. Thomas, C. Colin, P. Bertrand, L. Thivillon, et al., Adv. Mater. Res. 586 (2010) 89.
[30] X.P. Li, C.W. Kang, H. Huang, L.C. Zhang, T.B. Sercombe, Mater. Sci. Eng., A 606 (2014) 370–379.
[31] X.P. Li, C.W. Kang, H. Huang, T.B. Sercombe, Mater. Des. 63 (2014) 407–411.
[32] K.G. Prashanth, S. Scudino, H.J. Klauss, K.B. Surreddi, L. Löber, Z. Wang, A.K. Chaubey, U. Kühn, J. Eckert, Mater. Sci. Eng., A 590 (2014) 153–160.
[33] X.J. Wang, L.C. Zhang, M.H. Fang, T.B. Sercombe, Mater. Sci. Eng., A 597 (2014) 370–375.
[34] Z. Xiao, Y. Yang, X. Luo, B. Huang, Appl. Phys. Lett. (2014) 081611.
[35] R.C. Weast, S.M. Selby, CRC Handbook of Chemistry and Physics, CTC Press, 1981.
[36] L.K. Ang, Y.Y. Lau, R.M. Gilgenbach, H.L. Spindler, Appl. Phys. Lett. 70 (1997) 696–698.
[37] S.C. Stacy, X. Zhang, M. Pantoya, B. Weeks, Int. J. Heat Mass Transfer 73 (2014) 595–599.
[38] L. Thijs, K. Kempen, J.P. Kruth, J.V. Humbeeck, Acta Mater. 61 (2013) 1809–1819.
[39] M. Calvo-Dahlborg, P.S. Popel, M.J. Kramer, M. Besser, J.R. Morris, U. Dahlborg, J. Alloys Compd. 550 (2013) 9–22.
[40] W.D. Griffiths, D.G. McCartney, Mater. Sci. Eng., A 216 (1996) 47–60.
[41] S. Nafisi, D. Emadi, M.T. Shehata, R. Ghomashchi, Mater. Sci. Eng., A 432 (2006) 71–83.
[42] M. Gupta, E.J. Lavernia, J. Mater. Process. Technol. 54 (1995) 261–270.
[43] J. Wang, S. He, B. Sun, Q. Guo, M. Nishio, J. Mater. Process. Technol. 141 (2003) 29–34.
[44] I.G. Brodova, P.S. Popel, G.I. Eskin, in: J.N. Fridlyander, D.G. Eskin (Eds.), Liquid Metal Processing: Application to Aluminium Alloy Production, Advances in Metallic Alloys, Taylor & Francis, London, 2002.
[45] S. Katakam, J.Y. Hwang, H. Vora, S.P. Harimkar, R. Banerjee, N.B. Dahotre, Scripta Mater. 66 (2012) 538–541.
[46] X.P. Li, M. Roberts, Y.J. Liu, C.W. Kang, H. Huang, T.B. Sercombe, Mater. Des. 65 (2015) 1–6.
[47] W.D. Liu, L.M. Ye, K.X. Liu, J. Appl. Phys. 109 (2011). 043109-09-5.
[48] M. Asta, C. Beckermann, A. Karma, W. Kurz, R. Napolitano, M. Plapp, G. Purdy, M. Rappaz, R. Trivedi, Acta Mater. 57 (2009) 941–971.
[49] D. Qiu, M.-X. Zhang, J. Alloys Compd. 586 (2014) 39–44.
[50] J. Zhang, H. Yu, S.B. Kang, J.H. Cho, G. Min, V.Y. Stetsenko, J. Alloys Compd. 541 (2012) 157–162.
[51] K. Dai, L. Shaw, Acta Mater. 49 (2001) 4171–4181.
[52] G. Viera, S. Huet, L. Boufendi, J. Appl. Phys. 90 (2001) 4175–4183.
[53] Y. Chen, M. Weyland, C.R. Hutchinson, Acta Mater. 61 (2013) 5877–5894.